

Land-Use/Land-Cover Change Detection Based on Class-Prior Object-Oriented Conditional Random Field Framework for High Spatial Resolution Remote Sensing Imagery

Sunan Shi^{ID}, Yanfei Zhong^{ID}, Senior Member, IEEE, Ji Zhao^{ID}, Member, IEEE, Pengyuan Lv, Yinhe Liu, and Liangpei Zhang^{ID}, Fellow, IEEE

Abstract—High spatial resolution (HSR) remote sensing images can reflect more subtle changes and more specific types of land use and land cover (LULC) due to the abundant spatial geometric information. In this article, a class-prior object-oriented conditional random field (COCR) framework consisting of a binary change detection (CD) task and a multiclass CD task is proposed to fill the application gap. In the proposed framework, the class-prior knowledge is used to improve the construction of the unary potential in both the binary and multiclass CD tasks, to reduce the influence of spectral variability. The binary CD result provides a constraint to the multiclass CD result. As a result, both parts have effective interaction. The class posterior probability images of two dates can be obtained automatically with the class-prior knowledge by sample migration. Furthermore, an object constraint described by the class dispersion within the objects is added to improve the smoothness in local objects, while the pairwise potential improves the smoothness of the whole area by using the eight-neighborhood spectral information of the center pixel. By integrating the above approaches, the problems of error accumulation and the manual intervention required in the traditional multiclass CD methods can be relieved. An adaptive parameter estimation strategy is also adopted in the proposed framework, to save the time required for manual parameter setting. The proposed COCRF framework was validated on two HSR remote sensing image data sets, where it achieved a better performance than the other state-of-the-art CD methods.

Index Terms—Conditional random fields (CRFs), high spatial resolution (HSR), multiclass change detection (CD), object-oriented, remote sensing.

Manuscript received March 7, 2020; revised August 30, 2020; accepted October 3, 2020. This work was supported by the National Natural Science Foundation of China under Grant 41771385, Grant 42071350, and Grant 42001307. (*Corresponding author: Yanfei Zhong*.)

Sunan Shi, Yanfei Zhong, Yinhe Liu, and Liangpei Zhang are with the State Key Laboratory of Information Engineering in Surveying, Mapping and Remote Sensing, Wuhan University, Wuhan 430079, China, and also with the Hubei Provincial Engineering Research Center of Natural Resources Remote Sensing Monitoring, Wuhan University, Wuhan 430079, China (e-mail: shisunan@whu.edu.cn; zhongyanfei@whu.edu.cn; liuyinhe@whu.edu.cn; zlp62@whu.edu.cn).

Ji Zhao is with the College of Computer Science, China University of Geosciences, Wuhan 430079, China (e-mail: zhaoji@cug.edu.cn).

Pengyuan Lv is with the School of Information Engineering, Ningxia University, Yinchuan 750021, China (e-mail: lpydtc@nxu.edu.cn).

Color versions of one or more figures in this article are available at <https://doi.org/10.1109/TGRS.2020.3034373>.

Digital Object Identifier 10.1109/TGRS.2020.3034373

I. INTRODUCTION

CHANGE detection (CD) is aimed at identifying changes on the ground by analyzing multitemporal remote sensing images taken in the same geographical area at different dates [1]. CD has been recognized as being an increasingly important research topic in the remote sensing field because it plays an increasingly widespread role in various practical application domains, such as environmental monitoring [2], disaster assessment [3], [4], urban expansion [5], [6], and forest monitoring [7]. In the past few decades, remote sensing technology has developed rapidly, and numerous methods have been developed for land-use and land-cover (LULC) CD using remotely sensed data [8]. These methods can be broadly grouped into two categories—pixel-based CD (PBCD) [9], [10] and object-based CD (OBED) [11], [12]—according to their basic analysis units.

Classical CD methods such as image differencing [13], principal component analysis (PCA) [14], spectral gradient differencing [13], or change vector analysis (CVA) [9], [15] were generally implemented at the pixel level in the early stages. However, with the rapid development of Earth observation technology, more and more high spatial resolution (HSR) remote sensing images providing abundant detailed geometric information are becoming available for CD tasks [11]. The geometric information of these images becomes more obvious and subtle changes can be detected. At the same time, the pixel-based methods, which lead to a lot of “salt-and-pepper” noise, are no longer practicable due to the assumption of spatial independence among pixels [11], [16], [17]. Therefore, it is necessary to consider the spatial-contextual information in HSR images [18].

Object-based image analysis using spatial and spectral information is attracting more and more attention and has demonstrated great potential in image processing research [19]–[21]. For OBED methods, an object consisting of several pixels with similar spectral characteristics is considered as the minimum analysis unit, instead of a single pixel [20], [22]. OBED methods can be divided into different classes, i.e., postclassification comparison (PCC) methods and direct comparison (DC) methods [23], [24]. Object-based PCC (OBPCC) methods

first classify the input images into different LULC classes at the object level. The change maps describing the types of different change directions can then be obtained by comparing the classification maps produced independently for the two different dates [9]. Similar to the pixel-based PCC methods, the OBPCC methods minimize the noise caused by different sensors, vegetation phenology, sunlight, and atmospheric conditions [22], [25], but the final accuracy of the change map is still based on the product of the accuracies of the two classification maps obtained at different dates. In addition, the class labels of the two single images are also needed [26]. As a result, object-based DC (OBDC) methods always lead to change results with better accuracies [27]. Most pixel-based DC methods can be conducted at the object level and have been shown to eliminate salt-and-pepper noise very well for HSR images [28]. However, DC methods based only on the original remote sensing images are usually limited to a binary CD result, which only provides the change and no-change information.

As a consequence, many supervised DC methods based on prior data have been proposed to obtain multiclass CD results. Examples of such methods are direct classification relying on stacked multitemporal images [22], [29]–[31] and change analysis of changed areas combined with the updating or backdating of LULC mapping [26], [32], [33]. However, the former DC methods mentioned above always need a lot of manual intervention to label the samples of the “from-to” change information, while the latter methods require the use of fully labeled historical thematic maps, which can be difficult to obtain. All these supervised DC methods produce less error by eliminating the error accumulation resulting from two single classification maps, but they need more complex manually labeled prior data than the PCC-based methods. Either way, it is undeniable that multiclass CD is playing a more and more important role in various application fields [31] because the actual LULC transformations, which are closely related to the development of human society, can be reflected.

What is more, for most OBDC methods, there are basically two kinds of segmentation strategies for the object-level information [18], [34], [35]. On the one hand, the objects can be obtained by segmenting stacked multitemporal images [35]. On the other hand, the segmentation can be applied on the two registered images separately, and the final segmentation map is achieved by fusing the two segmentation maps via a logical “OR” operation [34]. However, the CD results are very sensitive to the segmentation scale and segmentation strategy, especially when the boundaries of the objects are clearly defined and analyzed [18], [22].

Aiming at this drawback, random field models, such as Markov random field (MRF) and conditional random field (CRF) models, are other popular ways to model the spatial information, in addition to the OBDC methods. MRF was first used for image processing in 1984 [36], and has since become widely used in CD [18], [37]. MRF-based methods consider the spatial-contextual information of the labeled image and build the joint distribution of the observed image and the change map using a Bayesian generative model [17], [38]. However, the MRF model implies some

assumptions about the images for computational tractability and, thus, may not be suitable for actual applications [39]. The CRF model directly modeling the posterior distribution is an improvement of MRF. The CRF-based methods are more flexible and can incorporate the spatial-contextual information in both the labels and observed data. Furthermore, the pairwise CRF model is the most common CRF model in remote sensing image processing tasks, such as segmentation, classification, and CD, so it has great potential in the development of multiclass CD research. The pairwise CRF model takes the spectral information as the unary potential and the contextual information of neighborhood pixels of a certain pixel as the pairwise potential [18], [38]. However, the traditional CRF-based methods are conducted at the pixel level, and the spatial information in the neighborhood does not come from a wide perspective. As a result, these methods are not really suitable for use with HSR images. To make better use of the spatial information at the object level, while reducing the negative influence of the objects’ boundaries, incorporating an object constraint into the traditional pairwise CRF model may be a sensible and reasonable approach [18].

Therefore, in this article, the class-prior object-oriented CRF (COCRF) framework consisting of a binary CD task and a multiclass CD task is proposed for HSR remote sensing imagery. The fuzzy object constraint improves the spatial-contextual learning ability, relative to the traditional CRF model. Furthermore, a semi-labeled class map is used as the prior knowledge to explore the class posterior probabilities of the two registered images so that the “from-to” change information can be estimated and the final CD result can show abundant change direction information. The main novel contributions of the COCRF framework are as follows.

- 1) The COCRF framework combining the binary and multiclass CD tasks is proposed. The unary potentials are differently constructed for the two tasks, while the pairwise potential and the object constraint of the proposed object-oriented CRF model are the same. The COCRF framework optimizes the binary CD task before the multiclass CD task. The binary CD task is constrained by the multiclass information through a similarity measurement of the class posterior probabilities, to decrease the inaccuracy caused by the use of only the spectral difference or the DC of class labels. The binary CD result provides a mask constraint when computing the “from-to” probability, so that only the changed areas are considered in the multiclass CD task. Furthermore, a joint optimization strategy based on task fusion in the unary potential of the object-oriented CRF model is also considered to generate a more lightweight framework.
- 2) To address the shortcoming of too much manual work being required in the supervised multiclass CD task, only a semi-labeled class map (the so-called “class prior”) of one date is needed in the proposed framework. Aiming at situations without sufficient historical data, we can label part of the image or even just the unchanged area. The sample migration can then be realized because the LULC classes should be the same in the unchanged areas. The class posterior probabilities are then obtained

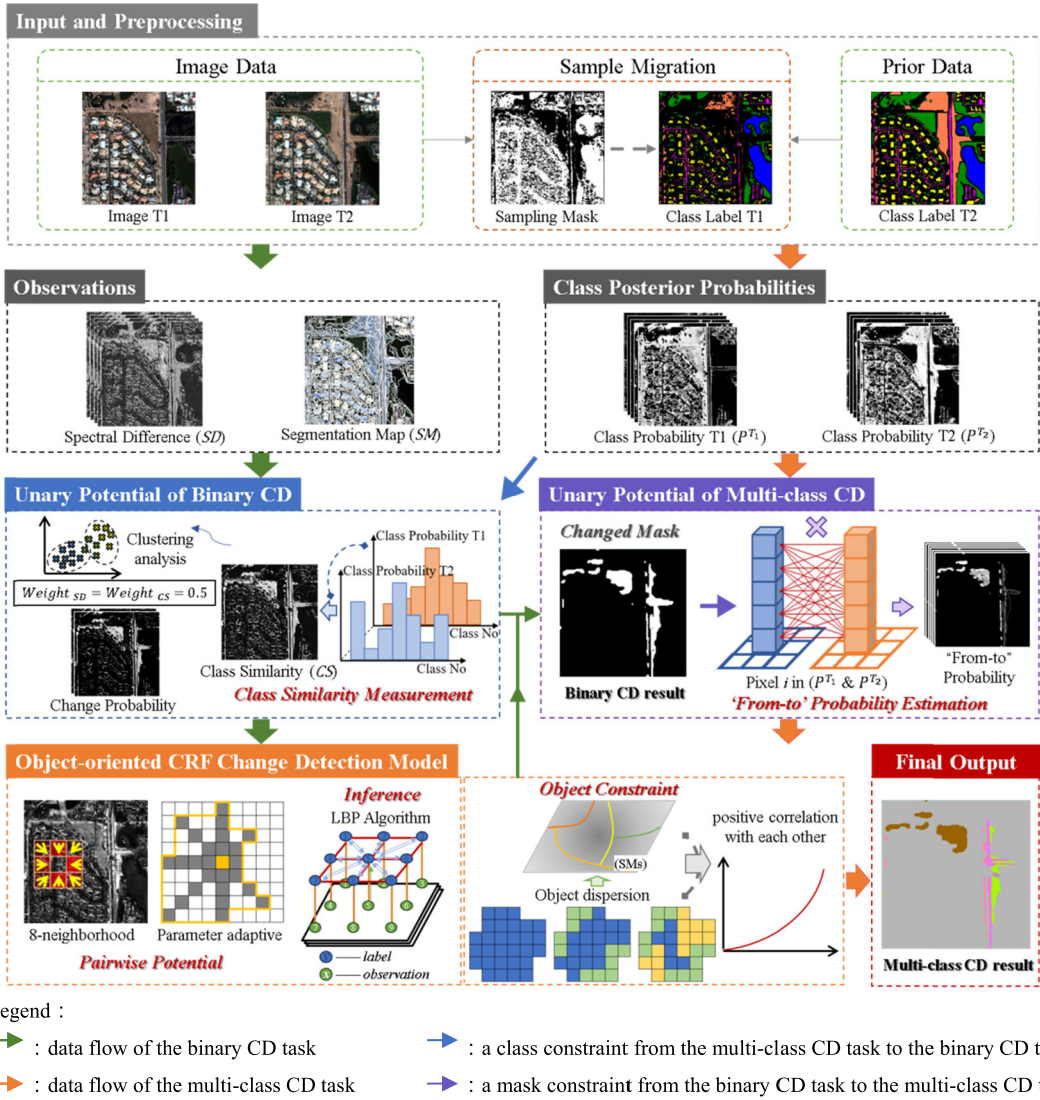


Fig. 1. Flowchart of the COCRF framework.

and shared in both tasks to improve the robustness of the final results. The parameters in most of the CRF models are set empirically, which require a lot of manual work. Therefore, an adaptive parameter estimation strategy is adopted in the proposed framework to reduce the run time.

- 3) To make full use of the spatial information and geographic structure of HSR images and take advantage of pixel interaction at the object level, an object constraint is incorporated into the pairwise CRF model. By analyzing the class dispersion degree within a single object, the strength of the object constraint is determined. The object constraint can reduce the impact of segmentation boundary errors to make the boundaries of the final results smoother and decrease the influence of the internal spectral variability of the objects.

The rest of this article is organized as follows. Section II details the proposed COCRF framework. Section III presents an alternative fusion strategy for the binary and multiclass CD tasks. Section IV gives a brief description of the study areas and the experimental results. A sensitivity analysis is

presented in Section V. Finally, the conclusions are drawn in Section VI.

II. PROPOSED CLASS-PRIOR OBJECT-ORIENTED CONDITIONAL RANDOM FIELD FRAMEWORK

The COCRF framework combining class-prior knowledge and an object constraint is proposed for HSR remote sensing imagery, to perform the binary and multiclass CD tasks. The CRF model is the core of the proposed framework, because it is a relatively mature model in the field of image classification and binary CD, and is suitable for the multiclass CD task with LULC classes. However, there is a difference between the unary potentials of CRF for the classification and binary CD tasks, which requires us to establish the unary potentials specifically for the binary and multiclass changes. The pairwise potential and the object constraint of the proposed object-oriented CRF model are same for the two tasks.

The COCRF framework optimizes the binary and multiclass CD tasks by constructing a mutual constraint of the two tasks on the data flow. As shown in Fig. 1, the flow arrows of the two

tasks are separately marked in green and orange. The binary CD task is optimized before the multiclass CD task. The unary potential of the multiclass CD task is constrained by the binary CD result so that the multiclass CD is only conducted in the changed areas of the binary CD result. A large number of false alarms (FAs) caused by classification errors can be eliminated and more robust results for different data sets can be generated with the proposed COCRF framework.

The data preparation for the COCRF framework consists of sample migration and the acquisition of observations and class posterior probabilities. The sample migration is conducted in unchanged areas because these LULC classes should be the same between the two dates. With the shared class labels acquired by sample migration, the class posterior probability images (P^{T_1} and P^{T_2}) for the two dates can be computed by any supervised classifier. The spectral difference map (\mathbf{x}^{SD}) and segmentation map (\mathbf{x}^{SM}) are separately obtained by the image differencing and the segmentation. With the prepared data, the similarity and the change direction of each pixel between the two dates can be estimated.

In order to obtain a binary CD result and a multiclass CD result, the unary potentials for the two tasks are generated separately to better illustrate the binary or multiclass changes. A clustering algorithm such as the fuzzy c-means (FCM) algorithm is used to obtain the change probability as the unary potential for the binary CD task. The unary potential of the multiclass CD task is the “from-to” probability estimated by the product of the class posterior probabilities. We do not adopt the PCC method but rather a direct classification strategy based on the “from-to” probability because the classification errors can be largely eliminated in this way.

The pairwise potential is modeled using an Ising model to consider the contextual information of both the observed and labeled fields. The loopy belief propagation (LBP) algorithm is used to deduce the final results. The spatial information learned by the traditional pairwise potential is limited for HSR images, so the homogeneity at larger or even different scales is considered by adding an object constraint which is suitable for both the binary and multiclass tasks at the same time. The pairwise potential, object constraint, and inference are all the same for the two tasks. Based on the COCRF framework, both binary and multiclass CD results with a low FA rate can be acquired.

A. Object-Oriented CRF Change Detection Model

CRF is a widely used discriminative probabilistic graphical model that is aimed at modeling the spatial relationship among pixels by the edge connection between neighborhoods [40]. Given an image with N pixels, the observations can be denoted by $\mathbf{x} = \{x_1, x_2, \dots, x_N\}$, where x_i represents the spectral feature of pixel i and $\mathbf{y} = \{y_1, y_2, \dots, y_N\}$ represents the labels of each pixel. The CRF model directly builds the posterior probabilities of the label image according to the following form [41], [42]:

$$P(\mathbf{y}|\mathbf{x}) = \frac{1}{Z(\mathbf{x})} \exp \left\{ - \sum_{l \in L} \psi_l(\mathbf{x}, \mathbf{y}_l) \right\} \quad (1)$$

where $Z(\mathbf{x}) = \sum_{\mathbf{y}} \exp \{- \sum_{l \in L} \psi_l(\mathbf{x}, \mathbf{y}_l)\}$ is the partition function, which is a normalization factor, and $\psi_l(\mathbf{x}, \mathbf{y}_l)$ denotes the potential function, such as a unary potential, pairwise potential, or even higher order potential functions. L represents the set of all the cliques.

The pairwise CRF model is commonly used for image processing due to its convenience in modeling and inference. The local discriminative information of each pixel is described by the unary potential, while the pairwise potential considers the spatial-contextual information of both the labeled and observed fields. Thus, the pairwise CRF model is described as follows:

$$P(\mathbf{y}|\mathbf{x}) = \frac{1}{Z(\mathbf{x})} \exp \left\{ \sum_{i \in N} \varphi_i(\mathbf{x}, y_i) + \sum_{i \in N} \sum_{j \in \eta_i} \phi_{ij}(\mathbf{x}, y_i, y_j) \right\} \quad (2)$$

where φ_i is the unary potential term. ϕ_{ij} is the pairwise potential, which focuses on the interaction of the neighborhood pixels defined by η_i . $Z(\mathbf{x})$ is the partition function.

The traditional pairwise CRF model is realized at the pixel level; however, the spatial learning ability is not deep enough for HSR images because the shape and size of different objects do vary greatly. In contrast, the OBCD methods can utilize the spatial information from a broader horizon or even different scales. In order to explore more spatial information while avoiding the negative influence of wrong segmentation boundaries, higher order CRF has been proposed and has achieved good performances at the object level by designing higher order potentials [18], [43]. Thus, the object constraint is designed as another potential function.

The proposed COCRF framework can be written as

$$P(\mathbf{y}|\mathbf{x}) = \frac{1}{Z(\mathbf{x})} \exp \left\{ \sum_{i \in N} \varphi_i(\mathbf{x}, y_i) + \lambda \sum_{i \in N} \sum_{j \in \eta_i} \phi_{ij}(\mathbf{x}, y_i, y_j) + \beta \sum_{s \in SM} \xi_s(\mathbf{x}, y_s) \right\} \quad (3)$$

where ξ_s is the additional object constraint varying with the class dispersion within objects. The weights of the neighborhood term and object constraint are controlled by two positive coefficients λ and β to adapt to different data sets.

B. Unary Potential

The unary potential represents the probability of a single pixel taking a particular label. For the binary CD task, it is always formulated by soft clustering methods in unsupervised strategies, while for the classification task, supervised methods are always adopted. In order to describe the binary and multiclass changes effectively, the unary potentials are separately constructed for the binary and multiclass tasks. The class posterior probabilities are first obtained and shared in both tasks to improve the robustness.

1) Class Posterior Probabilities of Two Dates Obtained by the Support Vector Machine Algorithm: The input data of the proposed framework are remote sensing images of two dates and a semilabeled map corresponding to one of

the dates. Due to the lack of changed samples, supervised CD approaches are difficult to implement. In order to make the prior knowledge fully serve the CD task, the class posterior probabilities of the two dates obtained by sample migration and support vector machine (SVM) are used to construct the unary potentials of both tasks. The unchanged areas have the same LULC classes on both dates, so the sample migration focuses more on the purity of the extracted unchanged area than its integrity. The traditional unsupervised CD methods have a high efficiency and can ensure the purity of the extracted unchanged areas. Therefore, the unchanged areas are first obtained through any simple unsupervised CD method, such as the combination of multiband differencing and k-means used in the proposed framework.

The complete class labels are input into SVM to calculate the class posterior probability image of the same date as the class labels, while the class labels in the unchanged areas are used as the training samples for SVM to calculate the class posterior probability image of another date.

2) Unary Potential of the Binary CD Task Obtained by the FCM Algorithm: FCM is adopted to obtain the unary potential for the binary CD task. The difference image is usually used as the input of FCM in unsupervised CRF to obtain the change probability, but this is easily influenced by the radiation difference. To make better use of the class-prior knowledge and to judge the change probability of a pixel from the perspective of LULC classes, the similarity of the SVM probability outputs (P^{T_1} and P^{T_2}) is used in the unary potential construction of the binary CD task. Thus, both the spectral difference and the class posterior probability similarity are used to describe the change probability by separately inputting them into the FCM algorithm and then summing over the outputs.

The class posterior probability of a certain pixel can be viewed as a normalized histogram distribution in the feature space. Therefore, the histogram distance can be used to estimate the similarity of the class posterior probabilities of each pixel between different dates. As shown in Fig. 2(a), it is possible that pixels actually belonging to the same class have different labels attached, due to the radiation difference on the different dates. The exact opposite situation is depicted in Fig. 2(b), where the red box represents the given class label. As a result, the similarity estimation strategy can eliminate the FAs in the CD result caused by accumulation of the classification error.

The commonly used histogram distance measurement methods include Kullback–Leibler (KL) divergence, the histogram intersection distance, intersection entropy, and so on. The G-statistic [44], as one of the histogram distance functions, does not require us to make any assumption about the histogram distribution, and is adopted in the proposed framework. The G-statistic is formulated as follows:

$$G(f, h) = 2 \left\{ \sum_{i=1}^L f^i \ln f^i + \sum_{i=1}^L h^i \ln h^i \right. \\ \left. + \left[\sum_{i=1}^L (f^i + h^i) \right] \ln \left[\sum_{i=1}^L (f^i + h^i) \right] \right\}$$

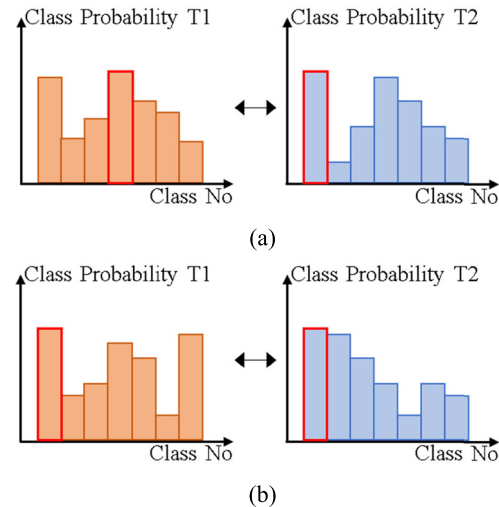


Fig. 2. Comparison of the class posterior probability distribution histograms. (a) Class labels are different but the histograms are very similar. (b) Class labels are the same but the histograms are clearly different.

$$-\left(\sum_{i=1}^L f^i \right) \ln \left(\sum_{i=1}^L f^i \right) - \left(\sum_{i=1}^L h^i \right) \ln \left(\sum_{i=1}^L h^i \right) \\ - \sum_{i=1}^L (f^i + h^i) \ln (f^i + h^i) \quad (4)$$

where f and h , respectively, stand for the two vectors of the class posterior probabilities that need to be compared, i represents the class that f or h may belong to, and L is the total number of compared classes. $G(f, h)$ denotes the similarity of f and h .

Therefore, the unary potential for the binary CD task is then constructed as an ensemble of the two change features

$$\varphi_i^B(\mathbf{x}, y_i) = \ln P(y_i = l | \mathbf{x}^{\text{SD}}, P^{T_1}, P^{T_2}) \quad (5)$$

$$P(y_i = l | \mathbf{x}^{\text{SD}}, P^{T_1}, P^{T_2}) = 0.5 * F(\mathbf{x}^{\text{SD}}) \\ + 0.5 * F(G(P^{T_1}, P^{T_2})) \quad (6)$$

where $P(y_i = l | \mathbf{x}^{\text{SD}}, P^{T_1}, P^{T_2})$ is the posterior probability of pixels being given the label $l \in \{0, 1\}$, and J denotes the FCM function. $G(P^{T_1}, P^{T_2})$ represents the similarity of the class posterior probabilities P^{T_1} and P^{T_2} .

3) Unary Potential of the Multiclass CD Task Obtained by the Probability Estimation: The class posterior probabilities of a certain pixel at different dates are independent of each other, satisfying the statistical independence assumption. As a result, the unary potential of the multiclass CD task can be considered as the product of the class posterior probabilities on two dates, according to the joint probability calculation rule. Thus, the unary potential of the multiclass CD task is defined as

$$\varphi_i^M(\mathbf{x}, y_i) = \ln \left(P^{T_1}(y_i^{T_1} = l_c^{T_1} | \mathbf{x}^{T_1}) * P^{T_2}(y_i^{T_2} = l_c^{T_2} | \mathbf{x}^{T_2}) \right) \quad (7)$$

where \mathbf{x}^{T_1} and \mathbf{x}^{T_2} separately stand for the original image on dates T_1 and T_2 , $P^{T_1}(y_i^{T_1} = l_c^{T_1} | \mathbf{x}^{T_1})$ represents the class posterior probability of pixels taking the label $l_c \in \{1, 2, \dots, C\}$

on date T_1 , and $P^{T_2}(y_i^{T_2} = l_c^{T_2} | \mathbf{x}^{T_2})$ corresponds to date T_2 . C is the number of classes.

C. Pairwise Potential

Analyzing HSR remote sensing images using a single pixel as the elementary unit leads to a lot of salt-and-pepper noise due to the spectral variability phenomenon. The pairwise potential in CRF is used to solve this problem by taking the neighborhood spatial information around the center pixel into consideration in both the labeled and observed fields. In order to smooth the noise and focus on the detailed contextual information at the same time [17], [40], the pairwise potential is calculated as

$$\phi_{ij}(\mathbf{x}, y_i, y_j) = \begin{cases} 1 + \exp\left\{-\frac{\|x_i^d - x_j^d\|^2}{2\sigma^2}\right\}, & y_i = y_j \\ 0, & y_i \neq y_j \end{cases} \quad (8)$$

where the value $\|x_i^d - x_j^d\|^2$ is the Euclidean distance (ED) between adjacent pixels i and j , and σ^2 is estimated as the mean value of the ED of all the pixels. As shown in the above formula, if the two adjacent pixels are labeled with different classes, the neighborhood information is ignored. If the class labels of the two pixels are the same, the more similar change features lead to greater neighborhood contributions. There is no limit to the number of classes, so the pairwise potential is applicable to both the binary and multiclass CD tasks. Here, an eight-neighborhood is considered to construct the spatial correlation of the center pixels.

D. Object Constraint

An object constraint is applied in the COCRF framework to reduce the FAs caused by spectral anomalies. The objects are acquired using a multiresolution segmentation approach conducted on the stacked multitemporal images, so that the objects in both images are consistent and have good homogeneity. The segmentation map $\mathbf{x}^{\text{SM}} = \{\mathbf{x}_s^{\text{SM}} | s = 1, 2, \dots, S\}$, where S is the number of segmented objects, is used to model the object constraint. The corresponding value of the segmentation map is defined by the binary or multiclass change probability of each pixel. The object constraint is determined according to the dispersion degree of the inner classes within the object.

With the unary potential, the change type of each pixel can be determined with the highest class posterior probability. Pixels with the same change type are grouped into an inner class $\mathbf{x}_{sc}^{\text{SM}}$ of the current object \mathbf{x}_s^{SM} . The inner class that contains the most pixels within an object is considered as the center class $\mathbf{x}_{so}^{\text{SM}}$ of the object, and y_{so} is the label of the center class.

The average class posterior probability of each inner class within a certain object is considered as the probability characteristic of each inner class. The G-statistic distance between each inner class $\mathbf{x}_{sc}^{\text{SM}}$ and the center class $\mathbf{x}_{so}^{\text{SM}}$ is obtained by the use of (4) to express the dispersion degree within the current object. The proportion of pixels contained in each inner class within the current object to the total pixels of the object is also used in the calculation of the object constraint.

The formulation of the object constraint is finally defined as follows:

$$\zeta_{sc}(\mathbf{x}^{\text{SM}}, y_{sc}) = \begin{cases} 1 - \exp\left\{-\frac{\sum_{c=1}^C G(x_{sc}^{\text{SM}}, x_{so}^{\text{SM}}) * R(x_{sc}^{\text{SM}})}{2\sigma^2}\right\}, & y_{sc} = y_{so} \\ 0, & y_{sc} \neq y_{so} \end{cases} \quad (9)$$

where $G(x_{sc}^{\text{SM}}, x_{so}^{\text{SM}})$ represents the distance between the class posterior probability vector of a certain inner class $x_{sc}^{\text{SM}} \in x_s^{\text{SM}}$ and the class posterior probability vector of the center class $x_{so}^{\text{SM}} \in x_s^{\text{SM}}$ within a certain object. $R(x_{sc}^{\text{SM}})$ is the proportion of the pixels in each inner class to the total pixels of the object, and C is the number of classes. y_{sc} marks the assignment position in the posterior probability vector of the object constraint to each inner class, which means that the object constraint works only if the channel y_{sc} is equal to the class label y_{go} of the object's center class.

The object constraint can decrease the spectral variability of the same class between different dates. If there is a greater distance between the inner classes and the center class of one object, it is considered that the object has greater spectral variability and requires a stronger object constraint. In addition, the object constraint is proportional to the number of pixels within each inner class. An inner class containing a small number of pixels is considered to have been incorrectly divided into the current object due to incorrect segmentation boundaries. Therefore, a weak object constraint can reduce the impact of segmentation boundary errors and make the boundaries of the final results smoother.

E. Inference and Parameter Estimation

A local approximation approach named LBP, which finds the optimal state of the labeled image with the maximum *a posteriori* (MAP) criterion, is used to map the final binary and multiclass CD results. LBP is flexible in the modeling and is performed by passing the updated message within the eight-connected neighborhood during the iterations [18], [45]. The node message and the edge message are separately initialized by the unary/object potentials and the pairwise potential. The final results can be generated by setting the label with the highest belief probability for each pixel. The COCRF framework inferred by LBP is defined as

$$P(\mathbf{y}|\mathbf{x}) \propto \prod_{i=1}^N \{\exp[\varphi_i(\mathbf{x}, y_i) + \beta \zeta_s(\mathbf{x}, y_s)] \prod_{j \in \eta_i} \exp[\lambda \phi_{ij}(\mathbf{x}, y_i, y_j)]\}. \quad (10)$$

In the COCRF framework, some parameters need to be estimated, including the segmentation scale and the weights of the pairwise potential and object constraint. To reduce the run time of selecting suitable parameters, an adaptive parameter estimation strategy is used to obtain the coefficient λ of the pairwise potential.

The coefficient β_{MCD} keeps the balance between the unary and pairwise potentials. When the spatial homogeneity of the

observed field between the center pixel and its neighborhood is higher, the coefficient R_{sc} should be greater, which means that the label of this pixel should have a higher probability of being consistent with the labels in the neighborhood. In this way, λ_{BCD} is adaptively set for each pixel. Anisotropic local polynomial approximation-based intersection of confidence intervals (LPA-ICIs) is adopted to obtain the adaptive coefficient β_{BCD} . LPA-ICI was first proposed in 2004 for image denoising [46]. Multidirectional sectorial neighborhood estimation is carried out for each pixel, according to the spectral similarity between the center pixel and the neighborhood pixels. The adaptive size of the sector for each direction is then selected by the ICI rule, so that the image denoising can be realized by weighted averaging of pixels within the anisotropic neighborhood calculated by anisotropic LPA-ICI [47]. Therefore, according to the number of pixels which have high spatial homogeneity with each center pixel obtained by anisotropic LPA-ICI, the coefficient λ_{MCD} can be calculated as shown in the following steps.

- 1) Define a set of search directions $\{\theta_d | \theta_d = 2d\pi / D, d = 0, 1, \dots, D - 1\}$ for each pixel, where D is the number of directions, which is 8 in this article.
- 2) A finite set of window size $H = \{h_1, h_2, \dots, h_K\}$ is then introduced, starting with a quite small h_1 to the largest h_K . The set H can be determined according to the image resolution and the complexity of the LULC distribution. In this framework, $H = \{1, 2, 3, 4, 5\}$ is suggested for both data sets.
- 3) A varying scale family of directional LPA convolution kernels $\{g_h, \theta_d\}_{h \in H}$ is used to obtain a corresponding set of directionally varying scale estimations $\{\gamma_h, \theta_d\}_{h \in H}$, where $\gamma_h, \theta_d = \mathbf{x} \otimes g_h, \theta_d$.
- 4) The ICI rule is used to select the adaptive scale $h^+(i, \theta_d)$ of each direction for each pixel according to the estimation $\{\gamma_h, \theta_d\}_{h \in H}$. The adaptive neighborhood area U_i^+ is then finally quantified as

$$U_i^+ = \sum_{d=0}^{D-1} h^+(i, \theta_d). \quad (11)$$

- 5) R_{sc} for each pixel is then defined as

$$\lambda_i = \frac{U_i^+ - \min(U_i^+)}{\max(U_i^+) - U_i^+}. \quad (12)$$

The coefficient β of the object constraint is the reciprocal of λ because a pixel with a lower pairwise potential requires a stronger object constraint to distinguish whether it should be smoothed.

To analyze the effect of the adaptive parameter estimation strategy, a nonadaptive COCRF (NACOCR) framework which uses manually set parameters was compared with the proposed COCRF framework. The segmentation scale is still set manually, but the framework is less sensitive to this parameter, which is proved in Section IV

III. ALTERNATIVE CRF FUSION STRATEGY FOR THE BINARY AND MULTICLASS CD TASKS

The binary CD task is executed before the multiclass CD task in the proposed COCRF framework, so that the

framework needs to execute the object-oriented CRF model twice, which takes double the time. Thus, a jointly optimized COCRF (JOCOCR) framework with the same components as the proposed COCRF framework but different processes is proposed by jointly optimizing both the binary and multiclass CD tasks. The object-oriented CRF model only needs to be run once because the two tasks are combined in the unary potential. The weight coefficients of the unary potentials of the two tasks are specified by the significance of the two unary potentials. The sum of the two weight coefficients is equal to one. Finally, the unary potential is an integration of the potentials of the binary and multiclass CD tasks

$$\varphi_i(x, y_i) = w_i \varphi_i^B(x, y_i) + (1 - w_i) \varphi_i^M(x, y_i) \quad (13)$$

$$w_i = \frac{\text{var}(\varphi_i^B(x, y_i))}{\text{var}(\varphi_i^B(x, y_i)) + \text{var}(\varphi_i^M(x, y_i))} \quad (14)$$

where w_i represents the confidence of each pixel for the potential of the binary CD task, which is calculated according to the variance of the probability distributions of the binary and multiclass CD tasks. The larger the variance of the binary CD probability distribution $\text{var}(\varphi_i^B(x, y_i))$, the higher the confidence for the potential of the binary CD task, and the lower the confidence for the potential of the multiclass CD task.

The JOCOCR framework needs less time and fewer parameters than the COCRF framework. However, the fusion of the unary potentials for the binary and multiclass CD tasks is completely unsupervised, so that there is no guarantee that a credible change probability or class posterior probability can be selected. Thus, the JOCOCR framework is less robust to different data sets and varying segmentation scales, which is shown in Section IV.

IV. EXPERIMENTS AND ANALYSIS

A. Experimental Description

Two sets of HSR remote sensing images with different spatial resolutions and geometric complexities, plus a class-labeled map, were used to evaluate the effectiveness of the proposed COCRF framework compared with the state-of-the-art CD methods. In addition, the NACOCR and JOCOCR frameworks were considered as alternative frameworks.

The segmentation map used for the object constraint was generated by multiresolution segmentation in eCognition, and the parameters for the shape and compactness were set as 0.2/0.8 for both data sets. The segmentation scales for the two data sets are listed in Table I. For the binary CD task, the proposed frameworks (i.e., NACOCR, COCRF, and JOCOCR) were compared with a pixel-based CD method [the Kittler and Illingworth (KI) algorithm] [18], [48], an object-based CD method (OBCD) [18], [49], the MRF model [15], [18], and a classical pairwise CRF method (CRF) [18]. The KI algorithm is a classical CD method that sets a global threshold for the difference image to obtain the binary change map. The OBCD method segments the multitemporal images using the watershed algorithm. The scale and merge level for the OBCD method were separately set as 5 and 90 for both data

TABLE I
PARAMETER SETTINGS OF THE RANDOM FIELD-BASED METHODS

Random field based methods	Parameter settings	
	Shiyan dataset	Hankou dataset
MRF	$\lambda_{BCD} = 1.2$	$\lambda_{BCD} = 2.8$
CRF_EM	$\lambda_{BCD} = 1.4$	$\lambda_{BCD} = 2.0$
PCC_PCRF	$\lambda_{BCD} = 3.6$	$\lambda_{BCD} = 5.4$
DC_PCRF	$\lambda_{BCD} = 3.9$	$\lambda_{BCD} = 6.0$
PCC_OCRF	$R_{sc} = 30; \lambda_{MCD} = 2.4; \beta_{MCD} = 5$	$R_{sc} = 50; \lambda_{MCD} = 6.0; \beta_{MCD} = 1$
DC_OCRF	$R_{sc} = 50; \lambda_{MCD} = 6.0; \beta_{MCD} = 5$	$R_{sc} = 50; \lambda_{MCD} = 5.7; \beta_{MCD} = 1$
NACOCRF	$R_{sc} = 10; \lambda_{BCD} = 4.2; \beta_{BCD} = 1; \lambda_{MCD} = 4.5; \beta_{MCD} = 1$	$R_{sc} = 30; \lambda_{BCD} = 0.9; \beta_{BCD} = 3; \lambda_{MCD} = 0.3; \beta_{MCD} = 1$
COCRF	$R_{sc} = 10$	$R_{sc} = 30$
JOCOCRF	$R_{sc} = 50$	$R_{sc} = 40$

sets [18]. The other steps of OBCD were all performed in ENVI 5.0. The pairwise potential weights of the two random field-based approaches (MRF and CRF) were set by sensitivity analysis [18].

For the multiclass CD task, the proposed frameworks were compared with a change analysis approach based on the integration of backdating and an object-based method (BOB) [26]. The BOB approach creates a class hierarchy and conducts feature extraction based on the binary CD map to obtain the multiclass CD result. A multiresolution segmentation approach is also used in this method. The segmentation scales for the two data sets were both set as 50 through trial and error.

The three proposed COCRF frameworks were also compared with global PCC and global DC based on pixel-based and object-oriented CRF models (PCC_PCRF, DC_PCRF, PCC_OCRF, DC_OCRF), without using the mask constraint of the binary CD result. The four experiments were conducted to analyze the significance of each module of the proposed framework. The parameters of the random field-based methods were manually set, according to the sensitivity analysis, as shown in Table I. In addition, we used the adaptive parameter estimation strategy for COCRF and JOCOCRF to verify the effectiveness of this approach, and the two frameworks were compared with NACOCRF using the manually set parameters.

For the quantitative analysis, five measurements are used to evaluate the accuracy of the binary CD results: FAs, missed alarms (MA), overall accuracy (OA), Kappa coefficient, and F1 score. FA is the number of pixels incorrectly classified as changed over the total number of unchanged pixels in the reference map. MA is the number of pixels incorrectly classified as unchanged over the total number of changed pixels in the reference map [50]. OA is the number of correctly classified pixels over the total number of pixels in the whole area. The F1 score is the harmonic mean of the precision and recall [51]. Kappa reflects the consistency between the CD results and the reference [20], [52]. OA and Kappa are also used in the multiclass CD task, due to the convention of classification accuracy measurement.

B. Experiment 1: Shiyan QuickBird Data Set

The two images in the first remote sensing data set were acquired by the QuickBird satellite in 2002 and 2004, with four multispectral bands of a 2.4-m spatial resolution. The study area is Shiyan city, Hubei province, China. The spatial size of the images is 250 × 250 pixels, as shown in Fig. 3(a) and (b). The class labels consisting of five LULC types—bare, vegetation, road, water, and building—were available for the year 2004, as shown in Fig. 3(c), but in fact the class labels for any date would be acceptable. In this data set, the main changes took place in the area with the LULC types of bare, vegetation, road, and water, with the change directions being mainly from bare to vegetation or other classes, and from other classes to bare. The reference maps for the binary and multiclass CD are given in Fig. 3(d) and (e), respectively.

The results of the different binary CD methods (KI, OBCD, MRF, CRF, NACOCRF, COCRF, and JOCOCRF) for the Shiyan QuickBird data set are displayed in Fig. 4. As shown in Fig. 4(a), the pixel-based KI method results in a lot of salt-and-pepper noise because the spatial information, which is important for HSR images, is not taken into consideration. OBCD reduces the noise, to some degree, but it also causes some blocks of FAs, as in the top left of Fig. 4(b), because too much confidence in object boundaries results in object-level errors. MRF acquires a smooth result, but numerous false detections are caused by over-smoothing at the same time because it does not consider the observed image. CRF improves on this, but as shown in Fig. 4(c)–(g), CRF combining the class-prior knowledge and object constraint performs the best of all. The results of NACOCRF and COCRF are similar because only the parameter setting strategy is different. As shown in Fig. 4(f), the unsupervised adaptive parameter estimation strategy not only saves a lot of time but also shows great robustness. The jointly optimized JOCOCRF framework achieves a very high accuracy for the binary CD task on this data set, as shown in Fig. 4(g). However, the completely unsupervised fusion of the binary and multiclass

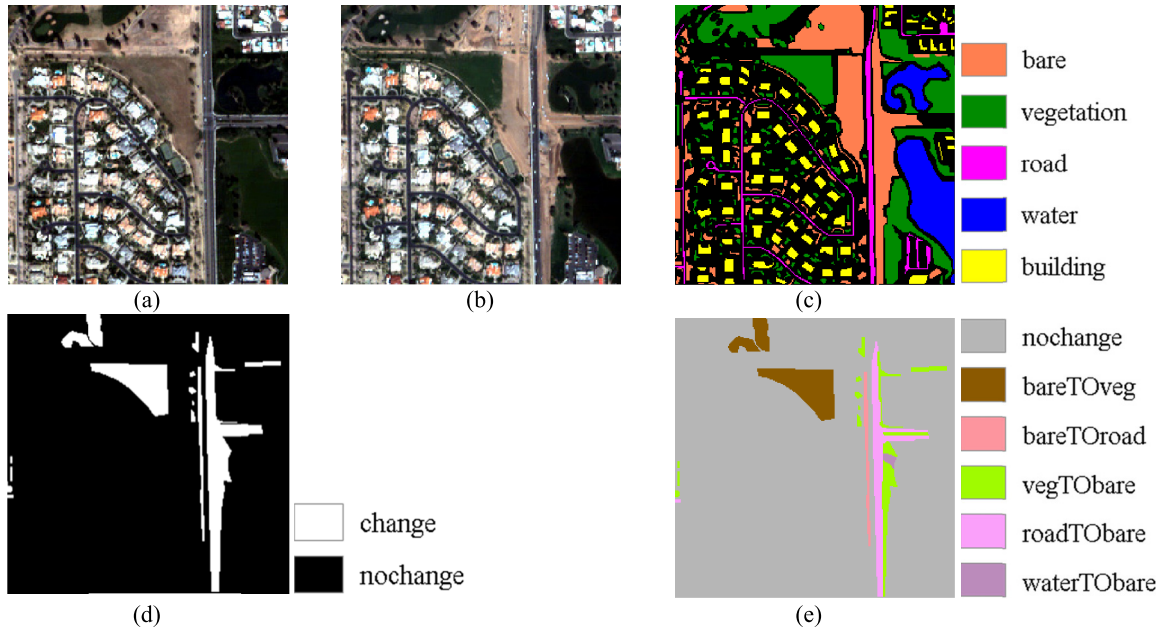


Fig. 3. Shiyan QuickBird data set. (a) Image taken in 2002. (b) Image taken in 2004. (c) Semi-labeled class map for 2004. (d) Binary CD reference map. (e) Multiclass CD reference map.

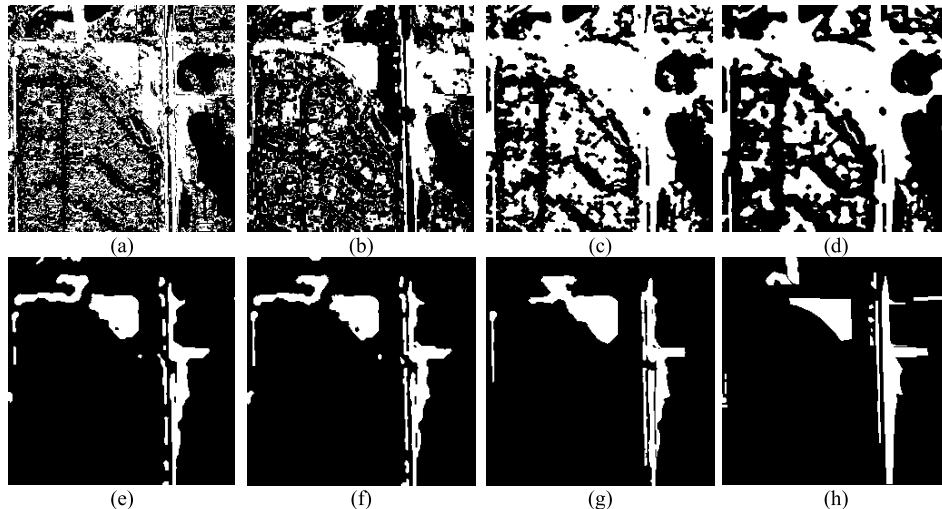


Fig. 4. Binary CD results for the Shiyan data set. (a) KI. (b) OBCD. (c) MRF. (d) CRF. (e) NACOCRF. (f) COCRF. (g) JOCOCRF. (h) Binary CD reference map.

CD potentials is easily affected by the correctness of the class posterior probability. Therefore, the reliability of JOCOCRF needs more verification on different data sets.

The quantitative results for the binary CD are listed in Table II. The spectral variability caused by different imaging conditions can lead to the phenomenon of changed pixels with a smaller spectral difference magnitude and unchanged pixels with a larger spectral difference magnitude, so that FAs or MAs occur. Taking the spatial-contextual information into consideration is an effective way to eliminate the noise. Not only does the spatial information assist in the three proposed frameworks using CRF and an object constraint, but the class information is also of great help. As a result, the F1 and Kappa values of the three COCRF frameworks are much higher than those of the other methods, which indicate that the proposed frameworks keep a better balance between FAs and MAs.

TABLE II
QUANTITATIVE RESULTS FOR THE SHIYAN
DATA SET IN THE BINARY CD TASK

Algorithm	FA(%)	MA(%)	OA(%)	Kappa	F1
KI [18]	35.52	9.87	66.95	0.2234	0.3444
OBCD [18]	27.18	16.50	73.85	0.2727	0.3808
MRF [18]	48.31	2.09	56.14	0.1645	0.3007
CRF [18]	38.34	2.18	65.14	0.2290	0.3509
NACOCRF	3.40	26.63	94.37	0.6837	0.7149
COCRF	3.45	25.98	94.38	0.6861	0.7173
JOCOCRF	3.48	26.00	94.35	0.6848	0.7161

The COCRF framework achieves the highest accuracy on the Shiyan data set, which indicates that the adaptive parameter estimation strategy is effective.

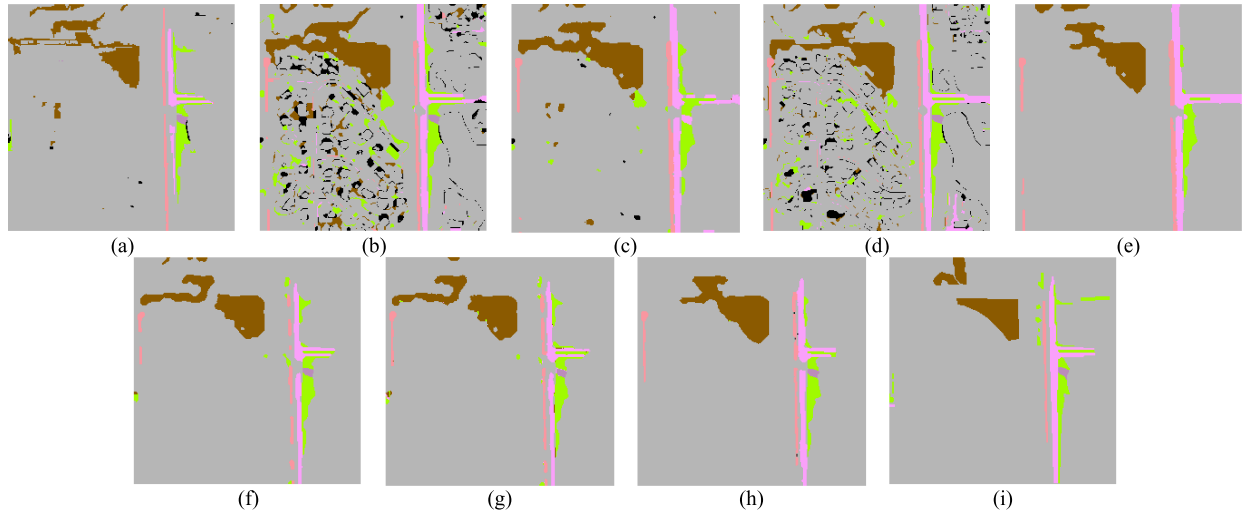


Fig. 5. Multiclass CD results for the Shiyan data set. (a) BOB. (b) PCC_PCRF. (c) DC_PCRF. (d) PCC_OCRF. (e) DC_OCRF. (f) NACOCRF. (g) COCRCF. (h) JOCOCRF. (i) Multiclass CD reference map.

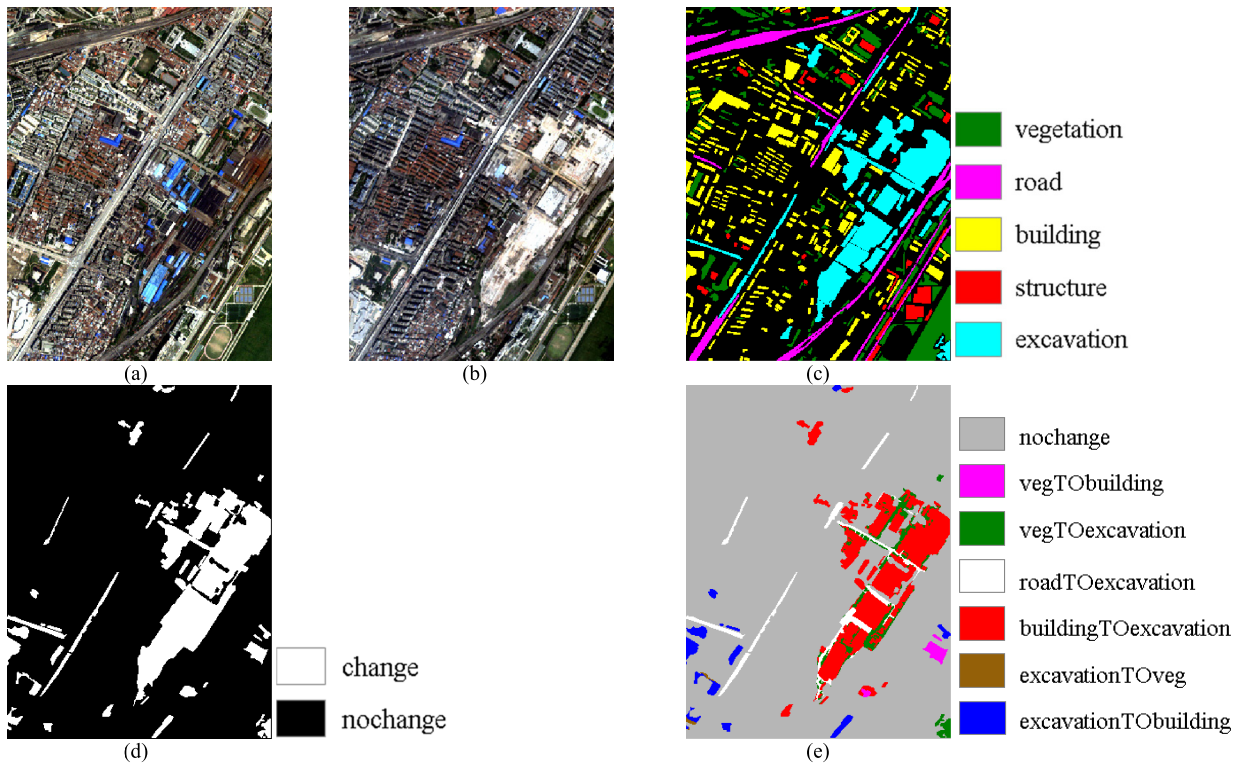


Fig. 6. Wuhan IKONOS data set. (a) Image taken in 2008. (b) Image taken in 2009. (c) Semi-labeled class map for 2009. (d) Binary CD reference map. (e) Multiclass CD reference map.

For the multiclass CD task, the proposed frameworks were compared with the BOB approach and four global PCC and CD methods based on pixel-based and object-oriented CRF models. The results are shown in Fig. 5. In addition to the classes contained in the reference image, some of the CD results contain classes not actually existing, which are marked in black. The BOB approach needs a class feature description for the other date in the changed area to obtain the classes so that a class comparison can be conducted to obtain the change directions. The BOB approach results in few FAs

because it analyzes at the object level and only in the changed areas. However, the BOB approach needs a lot of indices for feature description and extraction, so that it is not conducive to being generalized to other situations. It is shown by the results of the four module comparison experiments, as shown in Fig. 5(b)–(e), that both the object-oriented strategy and the direct classification approach can help to reduce the FAs of nonexistent “from-to” classes and pixels. The results of the proposed NACOCRF, COCRCF, and JOCOCRF frameworks show no detected change directions that do not exist in reality,

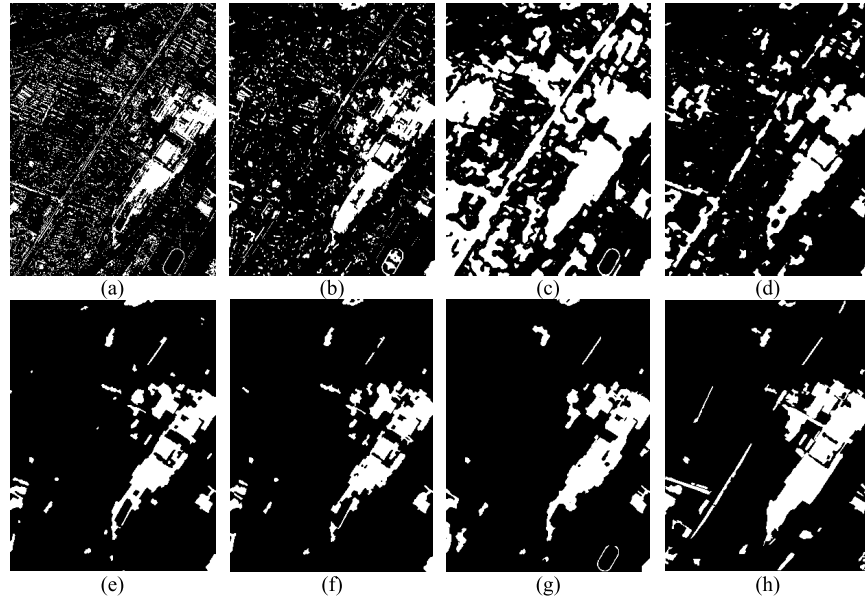


Fig. 7. Binary CD results for the Wuhan data set. (a) KI. (b) OBCD. (c) MRF. (d) CRF. (e) NACOCR. (f) COCRF. (g) JOCOCR. (h) Binary CD reference map.

TABLE III
QUANTITATIVE RESULTS FOR THE SHIYAN DATA SET IN THE MULTICLASS CD TASK

Algorithm	Object constraint	Prior knowledge		From-to probability estimation	Constrained by binary CD		Adaptive parameter estimation	OA(%)	Kappa
		Fully labeled class map	Semi-labeled class map		Sequential model	Joint model			
BOB [26]	✓	✓			✓			90.99	0.4970
PCC_PCRF			✓					82.27	0.4160
DC_PCRF			✓	✓				90.55	0.5746
PCC_OCRF	✓		✓					85.48	0.4556
DC_OCRF	✓		✓	✓				92.30	0.6251
NACOCR	✓		✓	✓	✓			94.10	0.6808
COCRF	✓		✓	✓	✓		✓	94.00	0.6777
JOCOCR	✓		✓	✓		✓	✓	94.10	0.6831

which is a significant improvement. The quantitative results for the multiclass CD task are listed in Table III. Overall, the proposed frameworks obtain the best performance, as in the visual results.

C. Experiment 2: Hankou IKONOS Data Set

To validate the proposed framework in a situation with more complex spatial geometric features, an HSR data set of a different sensor was used in the second experiment. The Wuhan urban area images with four multispectral bands of a 4-m spatial resolution were recorded by the IKONOS sensor over Wuhan in Hubei province, China, in 2008 and 2009. The spatial size of the images is 300 × 400 pixels, as shown in Fig. 6(a) and (b). The class labels consisting of five LULC types—vegetation, road, building, structure, and excavation—are available for the year 2009, as shown in Fig. 6(c). In this data set, the main change direction is from other classes to excavation. The reference maps for the binary and multiclass

CD are given in Fig. 6(d) and (e), respectively. This data set is more complex because the changes involve different artificial land uses, which may be made up of similar materials, so that the influence of “same material with different spectra” and “similar spectra from different materials” is greater.

The binary CD results (KI, OBCD, MRF, CRF, NACOCR, COCRF, and JOCOCR) for the Wuhan IKONOS data set are shown in Fig. 7, where it can be seen that the results show similar characteristics to the results for the Shiyan data set. As shown in Fig. 7(a), serious salt-and-pepper noise exists in the KI result because only the spectral difference is used. OBCD shows a good performance and reduces much of the noise, as a result of using the spatial information at the object level, but the degree of noise elimination depends on the segmentation scale. The MRF-based result contains a high level of FAs due to the over-smoothing, while CRF solves this problem by focusing on the observed field as well as the labeled field. The three proposed frameworks reduce

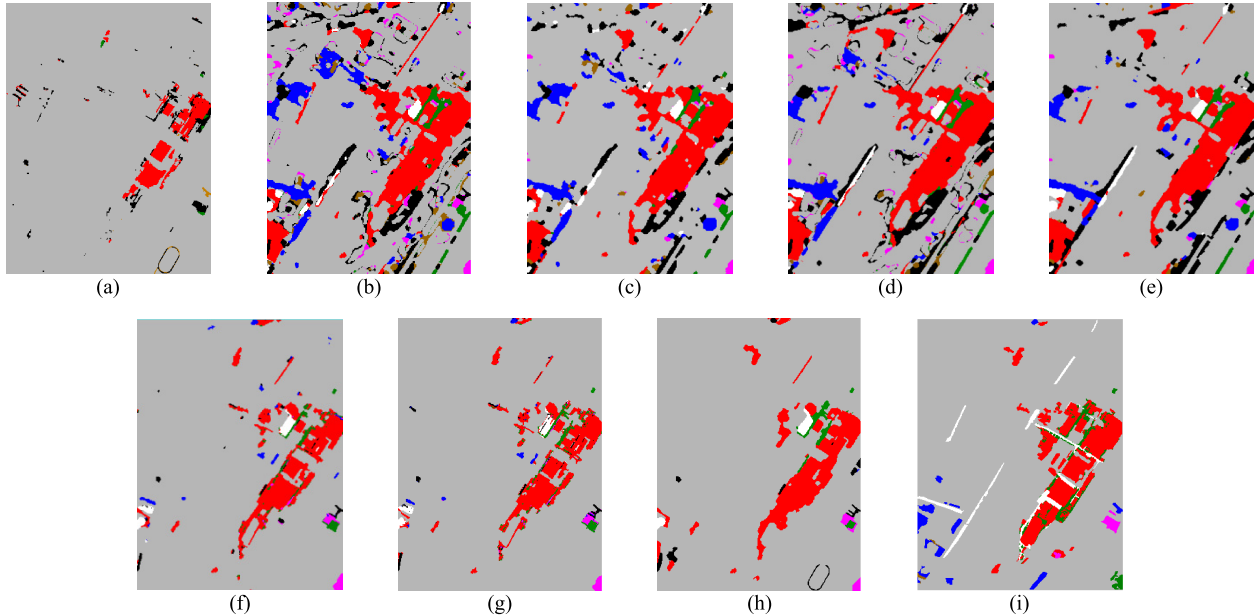


Fig. 8. Multiclass CD results for the Wuhan data set. (a) BOB. (b) PCC_PCRF. (c) DC_PCRF. (d) PCC_OCRF. (e) DC_OCRF. (f) NACOCRF. (g) COCRF. (h) JOCOCRF. (i) Multiclass CD reference map.

TABLE IV
QUANTITATIVE RESULTS FOR THE WUHAN DATA
SET IN THE BINARY CD TASK

Algorithm	FA(%)	MA(%)	OA(%)	Kappa	F1
KI [18]	9.67	44.24	85.38	0.4363	0.5221
OBCD [18]	7.10	38.02	88.47	0.5388	0.6063
MRF [18]	29.88	6.43	73.48	0.3709	0.5027
CRF [18]	7.81	21.98	90.18	0.6370	0.6947
NACOCRF	1.57	39.23	93.04	0.6761	0.7143
COCRF	1.18	41.64	93.03	0.6681	0.7057
JOCOCRF	2.10	39.48	92.54	0.6579	0.6992

the FAs to a great extent and show a better performance in detail, benefiting from the class-prior knowledge and the fuzzy object constraint. The adaptive parameter estimation strategy of COCRF has no obvious negative effect on the results, and it does save time when compared with NACOCRF.

The quantitative results for the five indices are listed in Table IV, where the results of JOCOCRF are not as good as those of the other two proposed frameworks, which implies that the unsupervised fusion of the binary and multiclass CD tasks has poor robustness to different data sets and is easily affected by the class posterior probability.

In the multiclass CD task, the BOB approach shows a few falsely detected change directions, as marked in black, but many change directions are wrongly assumed as unchanged at the same time, as shown in Fig. 8(a). This is because the materials of roads, buildings, and other artificial surfaces are difficult to distinguish, and they may be classified as the same class. The object-oriented strategies always achieve better results than the pixel-based strategies, especially for the CD of the objects' boundaries, which also holds true for the

previous experiments with the Shiyan data set. The proposed frameworks not only eliminate those change directions that do not exist in the multiclass CD reference map, but they also show a more comprehensive detection of the real change direction types, as shown in Fig. 8(f)–(h). The quantitative results are listed in Table V, where it can be seen that the results of the proposed frameworks are much better than the results of the other CD methods. The BOB approach shows a good performance in OA but leads to a low value in Kappa because lots of pixels are classified as unchanged. The accuracy of JOCOCRF is lower than that of NACOCRF and COCRF. Although the visual results of JOCOCRF are smoother, the wrong class posterior probabilities cause the correctly detected changed area to be assigned to wrong change directions. Therefore, the robustness of JOCOCRF should be further improved for different data sets, while COCRF obtains good results for both data sets and is more efficient and practical than NACOCRF.

V. SENSITIVITY ANALYSIS

The parameters denoted by λ and β play important roles in the proposed object-oriented CRF model, where λ is the weight of the pairwise potential and β is the weight of the object constraint. The two parameters control the smoothness of the whole area and the local objects, respectively. The object constraint comes from the segmentation maps, so that the segmentation scale is also an important parameter to be estimated. For all three proposed frameworks, the segmentation scale is selected by manual setting. Sensitivity curves for the segmentation scales are shown in Fig. 9. For the sequentially optimized frameworks of COCRF and NACOCRF, the segmentation scale is first determined for the binary CD task, and is then used in the multiclass CD task. The weights λ and β are set automatically by the adaptive

TABLE V
QUANTITATIVE RESULTS FOR THE WUHAN DATA SET IN THE MULTICLASS CD TASK

Algorithm	Object constraint	Prior knowledge		“From-to” probability estimation	Constrained by binary CD		Adaptive parameter estimation	OA(%)	Kappa
		Fully labeled class map	Semi-labeled class map		Sequential model	Joint model			
BOB [26]	✓	✓			✓			88.24	0.3607
PCC_PCRM				✓				75.08	0.3470
DC_PCRM				✓	✓			79.88	0.4074
PCC_OCRF	✓			✓				75.91	0.3576
DC_OCRF	✓			✓	✓			80.66	0.4177
NACOCRFR	✓			✓	✓	✓		90.21	0.5582
COCRF	✓			✓	✓	✓	✓	90.42	0.5569
JOCOCRFR	✓			✓	✓		✓	89.83	0.5467

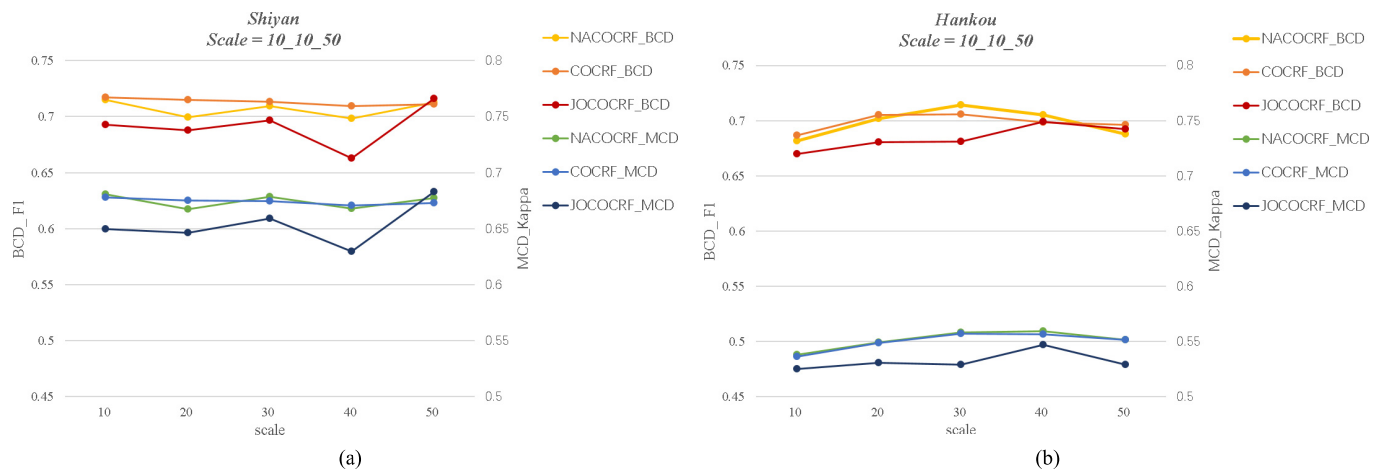


Fig. 9. Sensitivity analysis of the segmentation scale in the three proposed frameworks for the Shiyan and Wuhan data sets. (a) Shiyan data set. (b) Wuhan data set.

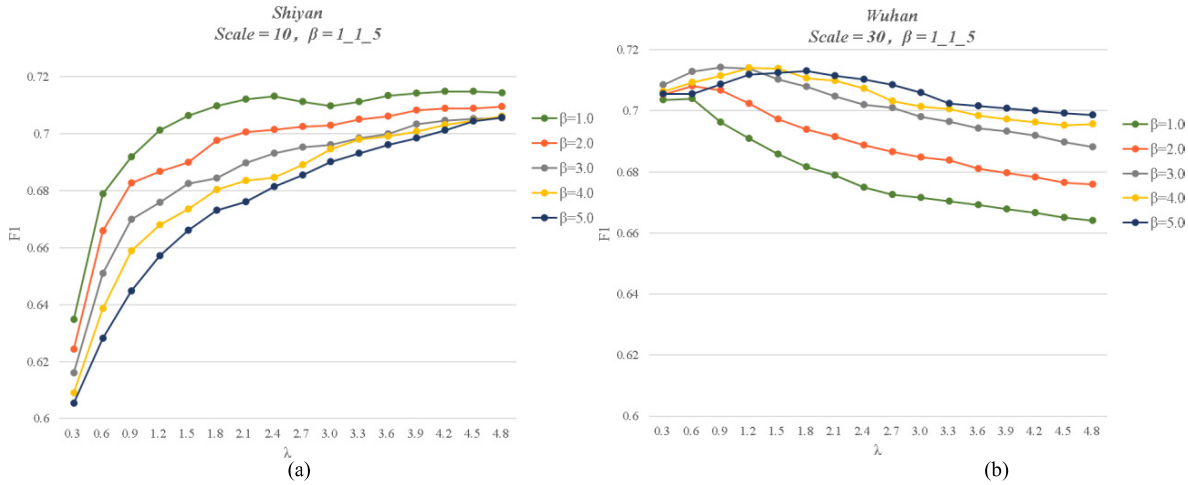


Fig. 10. Sensitivity analysis of parameters λ and β in the binary CD task of NACOCRFR for the Shiyan and Wuhan data sets under optimal segmentation scales. (a) Shiyan data set. (b) Wuhan data set.

parameter estimation strategy for COCRF and JOCOCRFR, while for NACOCRFR, λ and β are determined according to the sensitivity analysis. Figs. 10 and 11, respectively, show the sensitivity curves for these two parameters in both tasks of NACOCRFR under the optimal segmentation scale. The balance between MAs and FAs is important but difficult to

keep, because the numbers of pixels with different change directions are always uneven. To better evaluate the performance of the CD results, the F1 score is chosen as the index for the sensitivity analysis for the binary CD task, and the OA and Kappa are chosen for the multiclass CD task.

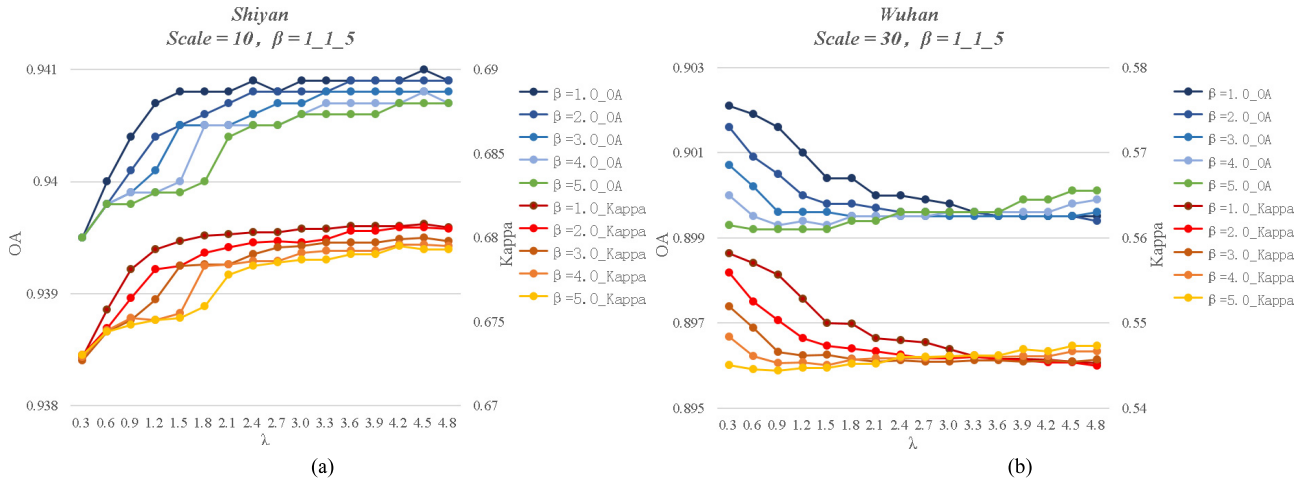


Fig. 11. Sensitivity analysis of parameters λ and β in the multiclass CD task of NACOCRF for the Shiyan and Wuhan data sets, with the segmentation scales decided by the binary CD task. (a) Shiyan data set. (b) Wuhan data set.

The segmentation scale was chosen from 10 to 50, with an interval of 10. Parameter λ was varied from 0.3 to 4.8, with an interval of 0.3. Parameter β was selected from 1 to 5, with an interval of 1. As shown in Fig. 9, the proposed sequentially optimized frameworks (NACOCRF and COCRF) are both robust to the segmentation scale. The index value of COCRF changes more gently as the segmentation scale increases, which means that the proposed COCRF framework is less sensitive to the segmentation scale, which is the only manually set parameter in COCRF. The sensitivity curves of the segmentation scales for JOCOCR for both data sets fluctuate more with the increase of the segmentation scale, which means that the appropriate segmentation scale needs to be selected for a certain practical application to achieve the ideal CD result. The sensitivity curves for λ and β with NACOCR under the optimal segmentation scale are shown in Figs. 10 and 11. The index value increases first and then decreases in the sensitivity analysis of the binary CD task because the process of noise elimination takes place first, and then transforms into over-smoothing with the increase of λ . The weight coefficient β of the object potential varies according to the different data sets and different segmentation scales, which brings difficulty to the manual setting. In the sensitivity analysis for the multiclass CD task, as shown in Fig. 11, the index value first increases and then decreases in the Shiyan data set, but decreases directly in the Wuhan data set, because the classes of the change direction in the Wuhan data set are subtle and the spatial constraint is weakened. Although the variations of λ and β have a certain regularity, the optimal ranges of the two parameters for the different data sets are clearly different. Therefore, the adaptive parameter estimation strategy is both necessary and of practical value.

VI. CONCLUSION

The COCRF framework with adaptive parameter estimation strategy has been proposed in this article to realize binary and multiclass CD for HSR remote sensing images. In addition, the NACOCR framework, which selects the parameters by

manual setting, and a jointly optimized JOCOCR framework have also been proposed in this article. For HSR remote sensing images, a large number of unsupervised algorithms have been proposed, but few of them focus on the multiclass CD task. Thus, our work addresses this application gap. The similarity of the class posterior probabilities is used, together with the spectral difference, in the construction of the unary potential, to acquire a more robust binary CD result, which was found to be superior to the results of the compared binary CD methods. The object constraint works for the proposed high-order CRF model so that the spatial correlation is considered at the object level and the noise is effectively eliminated. Finally, the change direction is detected by the probability estimation. In the NACOCR and COCRF frameworks, the binary CD result is used as a mask constraint, so that change directions that do not exist are not detected and FAs are greatly reduced. In the JOCOCR framework, the binary and multiclass CD tasks are fused in the unary potential, so that the binary and multiclass CD results can be obtained at the same time, which greatly improves the computational efficiency. Although the unsupervised fusion of the two tasks is less robust to different data sets, it has great research value. What is more, the adaptive parameter estimation strategy helps to obtain more robust results and saves a lot of work and time, which will be of great value in practical applications. All in all, the multiclass CD task is of great importance in various applications. In our future work, the application and potential of the multiclass CD task for HSR remote sensing images will be further explored. Unsupervised parameter setting and multitask fusion strategies, which should improve the efficiency of the model operation, will become our main research directions.

REFERENCES

- [1] A. Singh, "Review article digital change detection techniques using remotely-sensed data," *Int. J. Remote Sens.*, vol. 10, no. 6, pp. 989–1003, Jun. 1989.
- [2] A. Sih, M. C. O. Ferrari, and D. J. Harris, "Evolution and behavioural responses to human-induced rapid environmental change," *Evol. Appl.*, vol. 4, no. 2, pp. 367–387, Mar. 2011.

- [3] W. Shi and M. Hao, "A method to detect earthquake-collapsed buildings from high-resolution satellite images," *Remote Sens. Lett.*, vol. 4, no. 12, pp. 1166–1175, Dec. 2013.
- [4] L. Dong and J. Shan, "A comprehensive review of earthquake-induced building damage detection with remote sensing techniques," *ISPRS J. Photogramm. Remote Sens.*, vol. 84, pp. 85–99, Oct. 2013.
- [5] Q. Weng, "A remote sensing-GIS evaluation of urban expansion and its impact on surface temperature in the Zhujiang Delta, China," *Int. J. Remote Sens.*, vol. 22, no. 10, pp. 1999–2014, Jul. 2001.
- [6] A. Schneider, "Monitoring land cover change in urban and peri-urban areas using dense time stacks of Landsat satellite data and a data mining approach," *Remote Sens. Environ.*, vol. 124, pp. 689–704, Sep. 2012.
- [7] R. E. Kennedy, Z. Yang, and W. B. Cohen, "Detecting trends in forest disturbance and recovery using yearly Landsat time series: 1. LandTrendr-temporal segmentation algorithms," *Remote Sens. Environ.*, vol. 114, no. 12, pp. 2897–2910, Dec. 2010.
- [8] K. Cockx *et al.*, "Incorporating land-use mapping uncertainty in remote sensing based calibration of land-use change models," in *Proc. 8th Int. Symp. Spatial Data Quality Int. Arch. Photogramm. Remote Sens. Spatial Inf. Sci.*, 2013, pp. 7–12.
- [9] D. Lu, P. Mausel, E. Brondizio, and E. Moran, "Change detection techniques," *Int. J. Remote Sens.*, vol. 25, no. 12, pp. 2365–2407, Jun. 2004.
- [10] J. Chen, X. Chen, X. Cui, and J. Chen, "Change vector analysis in posterior probability space: A new method for land cover change detection," *IEEE Geosci. Remote Sens. Lett.*, vol. 8, no. 2, pp. 317–321, Mar. 2011.
- [11] J. Wu, B. Li, W. Ni, and W. Yan, "An adaptively weighted multi-feature method for object-based change detection in high spatial resolution remote sensing images," *Remote Sens. Lett.*, vol. 11, no. 4, pp. 333–342, Apr. 2020.
- [12] S. Toure *et al.*, "An object-based temporal inversion approach to urban land use change analysis," *Remote Sens. Lett.*, vol. 7, no. 5, pp. 503–512, May 2016.
- [13] J. Chen, M. Lu, X. Chen, J. Chen, and L. Chen, "A spectral gradient difference based approach for land cover change detection," *ISPRS J. Photogramm. Remote Sens.*, vol. 85, pp. 1–12, Nov. 2013.
- [14] J. S. Deng, K. Wang, Y. H. Deng, and G. J. Qi, "PCA-based land-use change detection and analysis using multitemporal and multisensor satellite data," *Int. J. Remote Sens.*, vol. 29, no. 16, pp. 4823–4838, Jul. 2008.
- [15] L. Bruzzone and D. F. Prieto, "Automatic analysis of the difference image for unsupervised change detection," *IEEE Trans. Geosci. Remote Sens.*, vol. 38, no. 3, pp. 1171–1182, May 2000.
- [16] Z. Li, W. Shi, H. Zhang, and M. Hao, "Change detection based on Gabor wavelet features for very high resolution remote sensing images," *IEEE Geosci. Remote Sens. Lett.*, vol. 14, no. 5, pp. 783–787, May 2017.
- [17] P. Lv, Y. Zhong, J. Zhao, H. Jiao, and L. Zhang, "Change detection based on a multifeature probabilistic ensemble conditional random field model for high spatial resolution remote sensing imagery," *IEEE Geosci. Remote Sens. Lett.*, vol. 13, no. 12, pp. 1965–1969, Dec. 2016.
- [18] P. Lv, Y. Zhong, J. Zhao, and L. Zhang, "Unsupervised change detection based on hybrid conditional random field model for high spatial resolution remote sensing imagery," *IEEE Trans. Geosci. Remote Sens.*, vol. 56, no. 7, pp. 4002–4015, Jul. 2018.
- [19] S. W. Myint, P. Gober, A. Brazel, S. Grossman-Clarke, and Q. Weng, "Per-pixel vs. object-based classification of urban land cover extraction using high spatial resolution imagery," *Remote Sens. Environ.*, vol. 115, no. 5, pp. 1145–1161, May 2011.
- [20] W. Feng, H. Sui, J. Tu, W. Huang, C. Xu, and K. Sun, "A novel change detection approach for multi-temporal high-resolution remote sensing images based on rotation forest and coarse-to-fine uncertainty analyses," *Remote Sens.*, vol. 10, no. 7, p. 1015, Jun. 2018.
- [21] Y. Zhang, D. Peng, and X. Huang, "Object-based change detection for VHR images based on multiscale uncertainty analysis," *IEEE Geosci. Remote Sens. Lett.*, vol. 15, no. 1, pp. 13–17, Jan. 2018.
- [22] M. Hao, W. Shi, K. Deng, H. Zhang, and P. He, "An object-based change detection approach using uncertainty analysis for VHR images," *J. Sensors*, vol. 2016, pp. 1–17, 2016.
- [23] M. Hussain, D. Chen, A. Cheng, H. Wei, and D. Stanley, "Change detection from remotely sensed images: From pixel-based to object-based approaches," *ISPRS J. Photogramm. Remote Sens.*, vol. 80, pp. 91–106, Jun. 2013.
- [24] G. Chen, G. J. Hay, L. M. T. Carvalho, and M. A. Wulder, "Object-based change detection," *Int. J. Remote Sens.*, vol. 33, no. 14, pp. 4434–4457, Jul. 2012.
- [25] W. Zhou, A. Troy, and M. Grove, "Object-based land cover classification and change analysis in the baltimore metropolitan area using multi-temporal high resolution remote sensing data," *Sensors*, vol. 8, no. 3, pp. 1613–1636, Mar. 2008.
- [26] W. Yu, W. Zhou, Y. Qian, and J. Yan, "A new approach for land cover classification and change analysis: Integrating backdating and an object-based method," *Remote Sens. Environ.*, vol. 177, pp. 37–47, May 2016.
- [27] D. Peng and Y. Zhang, "Object-based change detection from satellite imagery by segmentation optimization and multi-features fusion," *Int. J. Remote Sens.*, vol. 38, no. 13, pp. 3886–3905, Jul. 2017.
- [28] S. Bontemps, P. Bogaert, N. Titeux, and P. Defourny, "An object-based change detection method accounting for temporal dependences in time series with medium to coarse spatial resolution," *Remote Sens. Environ.*, vol. 112, no. 6, pp. 3181–3191, Jun. 2008.
- [29] B. Jeon and D. A. Landgrebe, "Classification with spatio-temporal interpixel class dependency contexts," *IEEE Trans. Geosci. Remote Sens.*, vol. 30, no. 4, pp. 663–672, Jul. 1992.
- [30] X. Dai and S. Khorram, "Remotely sensed change detection based on artificial neural networks," *Photogramm. Eng. Remote Sens.*, vol. 65, pp. 1187–1194, Oct. 1999.
- [31] S. Liu, D. Marinelli, L. Bruzzone, and F. Bovolo, "A review of change detection in multitemporal hyperspectral images: Current techniques, applications, and challenges," *IEEE Geosci. Remote Sens. Mag.*, vol. 7, no. 2, pp. 140–158, Jun. 2019.
- [32] X. Chen, J. Chen, Y. Shi, and Y. Yamaguchi, "An automated approach for updating land cover maps based on integrated change detection and classification methods," *ISPRS J. Photogramm. Remote Sens.*, vol. 71, pp. 86–95, Jul. 2012.
- [33] S. Jin, L. Yang, P. Danielson, C. Homer, J. Fry, and G. Xian, "A comprehensive change detection method for updating the national land cover database to Circa 2011," *Remote Sens. Environ.*, vol. 132, pp. 159–175, May 2013.
- [34] L. Ma *et al.*, "Change detection in optical remote sensing images with a fully object-level approach," in *Proc. IEEE Int. Geosci. Remote Sens. Symp. (IGARSS)*, Jul. 2018, pp. 1914–1917.
- [35] H. Sun, W. Zhou, Y. Zhang, C. Cai, and Q. Chen, "Integrating spectral and textural attributes to measure magnitude in object-based change vector analysis," *Int. J. Remote Sens.*, vol. 40, no. 15, pp. 5749–5767, Aug. 2019.
- [36] S. Geman and D. Geman, "Stochastic relaxation, Gibbs distributions, and the Bayesian restoration of images," *IEEE Trans. Pattern Anal. Mach. Intell.*, vol. PAMI-6, no. 6, pp. 721–741, Nov. 1984.
- [37] C. Benedek and T. Szirányi, "Change detection in optical aerial images by a multilayer conditional mixed Markov model," *IEEE Trans. Geosci. Remote Sens.*, vol. 47, no. 10, pp. 3416–3430, Oct. 2009.
- [38] J. Zhao, Y. Zhong, H. Shu, and L. Zhang, "High-resolution image classification integrating spectral-spatial-location cues by conditional random fields," *IEEE Trans. Image Process.*, vol. 25, no. 9, pp. 4033–4045, Sep. 2016.
- [39] T. Hoberg, F. Rottensteiner, R. Queiroz Feitosa, and C. Heipke, "Conditional random fields for multitemporal and multiscale classification of optical satellite imagery," *IEEE Trans. Geosci. Remote Sens.*, vol. 53, no. 2, pp. 659–673, Feb. 2015.
- [40] J. Zhao, Y. Zhong, and L. Zhang, "Detail-preserving smoothing classifier based on conditional random fields for high spatial resolution remote sensing imagery," *IEEE Trans. Geosci. Remote Sens.*, vol. 53, no. 5, pp. 2440–2452, May 2015.
- [41] J. Lafferty, A. McCallum, and F. C. Pereira, "Conditional random fields: Probabilistic models for segmenting and labeling sequence data," in *Proc. 18th Int. Conf. Mach. Learn.*, 2001, pp. 282–289.
- [42] S. Kumar and M. Hebert, "Discriminative random fields," *Int. J. Comput. Vis.*, vol. 68, no. 2, pp. 179–201, Jun. 2006.
- [43] P. Zhong and R. Wang, "Modeling and classifying hyperspectral imagery by CRFs with sparse higher order potentials," *IEEE Trans. Geosci. Remote Sens.*, vol. 49, no. 2, pp. 688–705, Feb. 2011.
- [44] A. Wang, S. Wang, and A. Lucieer, "Segmentation of multispectral high-resolution satellite imagery based on integrated feature distributions," *Int. J. Remote Sens.*, vol. 31, no. 6, pp. 1471–1483, Mar. 2010.
- [45] Y. Zhong, X. Lin, and L. Zhang, "A support vector conditional random fields classifier with a Mahalanobis distance boundary constraint for high spatial resolution remote sensing imagery," *IEEE J. Sel. Topics Appl. Earth Observ. Remote Sens.*, vol. 7, no. 4, pp. 1314–1330, Apr. 2014.
- [46] V. Katkovnik, A. Foi, K. Egiazarian, and J. Astola, "Directional varying scale approximations for anisotropic signal processing," in *Proc. 12th Eur. Signal Process. Conf.*, Sep. 2004, pp. 101–104.

- [47] A. Foi, V. Katkovnik, and K. Egiazarian, "Pointwise shape-adaptive DCT for high-quality denoising and deblocking of grayscale and color images," *IEEE Trans. Image Process.*, vol. 16, no. 5, pp. 1395–1411, May 2007.
- [48] F. Melgani, G. Moser, and S. B. Serpico, "Unsupervised change detection methods for remote sensing images," *Opt. Eng.*, vol. 41, no. 12, pp. 211–222, Dec. 2002.
- [49] I. Niemeyer, P. R. Marpu, S. Nussbaum, T. Blaschke, S. Lang, and G. J. Hay, "Change detection using object features," in *Object-Based Image Analysis*. Berlin, Germany: Springer-Verlag, 2008, pp. 185–201.
- [50] Z. Yetgin, "Unsupervised change detection of satellite images using local gradual descent," *IEEE Trans. Geosci. Remote Sens.*, vol. 50, no. 5, pp. 1919–1929, May 2012.
- [51] A. M. Lal and S. M. Anoucina, "Semi-supervised change detection approach combining sparse fusion and constrained k means for multi-temporal remote sensing images," *Egyptian J. Remote Sens. Space Sci.*, vol. 18, no. 2, pp. 279–288, Dec. 2015.
- [52] R. G. Congalton, "A review of assessing the accuracy of classifications of remotely sensed data," *Remote Sens. Environ.*, vol. 37, no. 1, pp. 35–46, Jul. 1991.



Sunan Shi received the B.S. degree from the School of Geosciences and Info-Physics, Central South University, Changsha, China, in 2018. She is pursuing the M.S. degree in photogrammetry and remote sensing with the State Key Laboratory of Information Engineering in Surveying, Mapping and Remote Sensing, Wuhan University, Wuhan, China.

Her research interests include unsupervised high-resolution remote sensing image change detection and land-cover and land-use change analysis.



Yanfei Zhong (Senior Member, IEEE) received the B.S. degree in information engineering and the Ph.D. degree in photogrammetry and remote sensing from Wuhan University, Wuhan, China, in 2002 and 2007, respectively.

Since 2010, he has been a Full Professor with the State Key Laboratory of Information Engineering in Surveying, Mapping and Remote Sensing (LIESMARS), Wuhan University. He organized the Intelligent Data Extraction, Analysis and Applications of Remote Sensing (RSIDEA) research group.

He has authored more than 100 research articles in international journals, such as the *Remote Sensing of Environment*, the *ISPRS Journal of Photogrammetry and Remote Sensing*, and the *IEEE TRANSACTIONS ON GEOSCIENCE AND REMOTE SENSING*. His research interests include hyperspectral remote sensing information processing, high-resolution remote sensing image understanding, and geoscience interpretation for multisource remote sensing data and applications.

Dr. Zhong is a Fellow of the Institution of Engineering and Technology (IET). He was a recipient of the 2016 Best Paper Theoretical Innovation Award from the International Society for Optics and Photonics (SPIE). He won the Second-Place Prize in 2013 IEEE GRSS Data Fusion Contest and the Single-view Semantic 3-D Challenge of the 2019 IEEE GRSS Data Fusion Contest, respectively. He is serving as an Associate Editor for the IEEE JOURNAL OF SELECTED TOPICS IN APPLIED EARTH OBSERVATIONS AND REMOTE SENSING, and the *International Journal of Remote Sensing*.



Ji Zhao (Member, IEEE) received the Ph.D. degree in photogrammetry and remote sensing from the State Key Laboratory of Information Engineering in Surveying, Mapping, and Remote Sensing, Wuhan University, Wuhan, China, in 2017.

He is an Associate Professor with the School of Computer Science, China University of Geosciences, Wuhan. His major research interests include high-resolution remote sensing image classification, scene analysis, remote sensing applications, and machine learning algorithms.



Pengyuan Lv received the B.S. degree in remote sensing and the Ph.D. degree in photogrammetry and remote sensing from Wuhan University, Wuhan, China, in 2013 and 2019, respectively.

He is working with the School of Information Engineering, Ningxia University, Yinchuan, China. His major research interests include high spatial resolution remote sensing image change detection, multitemporal image analysis, and random field algorithms.



Yinhe Liu received the B.S. degree from the School of Resources and Civil Engineering, Northeastern University, Shenyang, China, in 2019. He is pursuing the M.S. degree in photogrammetry and remote sensing with the State Key Laboratory of Information Engineering in Surveying, Mapping and Remote Sensing, Wuhan University, Wuhan, China.

His research interests include large-scale land-cover and land-use mapping and high-resolution remote sensing image processing.



Liangpei Zhang (Fellow, IEEE) received the B.S. degree in physics from Hunan Normal University, Changsha, China, in 1982, the M.S. degree in optics from the Xi'an Institute of Optics and Precision Mechanics, Chinese Academy of Sciences, Xi'an, China, in 1988, and the Ph.D. degree in photogrammetry and remote sensing from Wuhan University, Wuhan, China, in 1998.

He was a Principal Scientist for the China state key basic research project from 2011 to 2016 appointed by the ministry of national science and technology of China to lead the remote sensing program in China. He is a Chair Professor with the State Key Laboratory of Information Engineering in Surveying, Mapping, and Remote Sensing (LIESMARS), Wuhan University. He has authored more than 700 research articles and five books. He is the Institute for Scientific Information (ISI) highly cited author. He holds 30 patents. His research interests include hyperspectral remote sensing, high-resolution remote sensing, image processing, and artificial intelligence.

Dr. Zhang is a Fellow of the Institution of Engineering and Technology (IET). He was a recipient of the 2010 Best Paper Boeing Award, the 2013 Best Paper ERDAS Award from the American Society of Photogrammetry and Remote Sensing (ASPRS), and 2016 Best Paper Theoretical Innovation Award from the International Society for Optics and Photonics (SPIE). His research teams won the top three prizes of the IEEE GRSS 2014 Data Fusion Contest, and his students have been selected as the winners or finalists of the IEEE International Geoscience and Remote Sensing Symposium (IGARSS) student paper contest in recent years. He also serves as an Associate Editor or an Editor of more than ten international journals. He is serving as an Associate Editor of the *IEEE TRANSACTIONS ON GEOSCIENCE AND REMOTE SENSING*. He is the Founding Chair of the IEEE Geoscience and Remote Sensing Society (GRSS) Wuhan Chapter.